

# A Time-Dependent Ginzburg-Landau Framework for Sample-Specific Simulation of Superconductors for SRF Applications

Aiden V. Harbick\* and Mark K. Transtrum†

*Department of Physics and Astronomy, Brigham Young University, Provo, Utah 84602, USA*

(Dated: October 25, 2024)

Modern superconducting radio frequency (SRF) applications require precise control of a wide range of material properties, from microscopic material parameters to mesoscopic/macrosopic surface structures. Mesoscopic simulation of superconductors has proven itself to be a powerful tool in SRF development, connecting microscopic properties to the mesoscopic structures of the material. We outline a Time-Dependent Ginzburg-Landau (TDGL) framework which combines both experimental measurements and theoretical estimations of the properties of realistic sample materials into spatially varying TDGL parameters. We also derive a way to estimate SRF quality factors from TDGL solutions. We demonstrate an application of this framework by modeling Sn-deficient islands in Nb<sub>3</sub>Sn samples. We calculate the dissipation due to interactions of the superconducting order parameter and electromagnetic fields with these defects and estimate the impact to SRF cavity quality factor.

## I. INTRODUCTION

Superconducting Radio-Frequency (SRF) cavities are a crucial component of particle accelerators, as they utilize AC electromagnetic fields to accelerate beams of charged particles. Nb has been the industry standard for SRF applications for decades due to its high critical temperature ( $\sim 9\text{K}$ ) relative to the other elemental superconductors. Within the past decade, the need for SRF cavities with capabilities beyond the limits of Nb cavity performance has led to the study of a variety of alternative SRF materials. Among these materials, Nb<sub>3</sub>Sn has emerged as a promising candidate; Nb<sub>3</sub>Sn boasts both a higher critical temperature ( $\sim 18\text{K}$ ) and higher critical fields [1, 2]. One particular advantage of SRF cavities (as compared to traditional normal conducting RF cavities) is their high quality factors (Q) [3]. A major benefit of Nb<sub>3</sub>Sn SRF cavities compared to their Nb counterparts is that they can maintain similar Qs (on the order of  $10^{10}$ ) at higher temperatures (4.2K vs. 2K) [2], significantly reducing cryogenic costs. NbZr is another promising alternative SRF material which has seen recent attention [4, 5], with most existing NbZr samples exhibiting critical temperatures between 10 and 13K (the theoretical maximum is 17.7K), but this material has not yet been tested at cavity scale. The simulations in this paper focus on Nb<sub>3</sub>Sn, but the methods we will present can be generalized to any material of interest.

The oscillating electric fields used for acceleration in SRF cavities induce magnetic fields parallel to the cavity surface, so for large accelerating gradients, the critical magnetic fields of the cavity material are the fundamental limits on cavity performance. Type-II superconductors such as Nb and Nb<sub>3</sub>Sn have two critical fields,  $H_{c1}$  and  $H_{c2}$ . For fields below  $H_{c1}$ , the Meissner state is

stable and magnetic flux is expelled from the cavity. Between  $H_{c1}$  and  $H_{c2}$ , there is a mixed state in which superconducting vortices trap lines of magnetic flux, forming normal cores inside the otherwise superconducting state. Under an AC field, as is the case for SRF cavities, the vortices quickly move in and out of the cavity over the course of an AC cycle. This vortex motion leads to large amounts of dissipation [6]. For fields above  $H_{c2}$ , the mixed state becomes unstable and in this state SRF cavities will quench (i.e. go normal conducting). It is important to note that this is not the only mechanism for SRF cavity quench, the dissipation caused by moving vortices in the mixed state can cause heating in the cavity, which can also lead to quenching through a change in cavity temperature. As such, for SRF applications, it is important that the cavity remain within the Meissner state during operation.

While the Meissner state is no longer thermodynamically stable above  $H_{c1}$ , it can remain metastable up until the so-called superheating field,  $H_{sh}$  [7]. It is well known that most high-power SRF cavities operate in this metastable Meissner state [8]. As such,  $H_{sh}$  is the theoretical limiting field for operation of SRF cavities, since the dissipative vortices which are detrimental to SRF performance become unavoidable for fields above  $H_{sh}$ .  $H_{sh}$  has been studied for decades by condensed matter theorists. These studies have most commonly been within a Ginzburg-Landau (GL) framework [9–12], but the superheating field has also been studied extensively utilizing the Eilenberger equations [13–15].

$H_{sh}$  provides the maximum possible field (and therefore the maximum accelerating gradient) for SRF cavity operation, but local features of a material such as impurities or surface geometries can act as nucleation sites for vortices. This means that in practice, realistic material samples will be limited by what we will call the vortex penetration field,  $H_{vort}$ , which is the lowest field at which the material nucleates vortices. This quantity can vary greatly between different samples and depends on a large variety of different effects, so estimation of  $H_{vort}$  for re-

\* aharbick@student.byu.edu

† mktranstrum@byu.edu

alistic sample materials remains a rich area of research. For the case of Nb<sub>3</sub>Sn in particular, theoretical  $H_{sh}$  calculations suggest that Nb<sub>3</sub>Sn cavities could reach accelerating gradients as high as around 100 MV/m, yet the highest accelerating field achieved so far by a Nb<sub>3</sub>Sn SRF cavity is around 24 MV/m [16], with most other cavities reaching their quench field well below this. Additionally, many existing cavities exhibit a phenomenon in which Q significantly degrades as the cavity approaches its quench field, a phenomenon dubbed “Q-slope” [17], also sometimes called high field Q-slope (HFQS) when it occurs primarily at higher fields near the quench field. These performance degradations are the result of material defects introduced during the Nb<sub>3</sub>Sn growth process, so understanding how different defects seen within samples affect things like  $H_{vort}$  or dissipation more generally is critical to developing better growth techniques.

The need to accurately model specific features such as material impurities within superconducting materials motivates us to develop a framework which will allow us to directly model the spatial variations of superconducting properties due to the material compositions observed in realistic sample materials. To do this, we use time-dependent Ginzburg-Landau (TDGL) theory. TDGL has already proven itself to be a powerful tool for mesoscopic-scale simulations relevant to SRF applications [18–21]. Besides SRF simulations, TDGL has broad application such as in single photon detectors [22, 23], superconducting quantum interference devices (SQUIDs) [24, 25], weak links [26–30], or superconducting nanowires [31–33].

TDGL is a mesoscopic-scale model which abstracts the microscopic details of superconductivity into quantities which can be used to describe things like vortex dynamics. To model sample specific materials in order to understand the mechanisms behind Q-slope or other cavity quenching phenomena in Nb<sub>3</sub>Sn SRF cavities, we will make use of both experimental and theoretical work which has been performed to analyze the microscopic properties of Nb<sub>3</sub>Sn.

There has been a large body of work experimentally characterizing SRF grade vapor-diffused Nb<sub>3</sub>Sn samples. The primary suspect for SRF performance degradation comes from defects or other imperfections in the Nb<sub>3</sub>Sn surface significantly lowering the barrier to flux penetration [34]. In particular, defects which have been studied are abnormally thin or patchy grains [35–37], Sn-segregated grain boundaries [19, 38, 39], and Sn-deficient regions [35, 36, 40, 41]. In addition to experimental characterizations, there have also been a variety of *ab initio* calculations for Nb<sub>3</sub>Sn using density functional theory. In addition to calculations of general properties of Nb<sub>3</sub>Sn [42], such as the electron and phonon density of states and Eliashberg spectral function, these quantities have also been estimated with respect to varying intrinsic strain [43] as well as normal resistivity [44]. Variations in the superconducting  $T_c$  as well as electron density of states have also been calculated with respect to varying tin concentration [45, 46], which applies to both Sn-

segregation at grain boundaries and Sn-deficient regions. These Sn-deficient regions, or Sn-deficient islands as we will call them, are the primary material defect we will study in order to validate our methods.

Experimental characterizations can give data about the material compositions and physical structure of superconducting materials, and *ab initio* calculations provide detailed descriptions of the electronic/phononic structure and the resulting superconducting properties, both of these a microscopic scale. TDGL plays the role of modeling mesoscopic scale phenomena (such as vortex dynamics) which are difficult or even impossible to measure directly via experiment, and are too large to easily model with microscopic scale theories such as DFT. There have been a number of studies which have used TDGL to model material inhomogeneities [18, 19, 47–51], but these studies did not incorporate precise values of the TDGL parameters from microscopic material models. The limitation to the approach used in these references is that it requires either looking through a large portion of the TDGL parameter space in order to find values which lead to expected predictions, or more commonly, picking somewhat arbitrary values, which limits confidence in the results.

In this paper, we outline a new framework in TDGL theory which allows us to directly calculate the values of the TDGL parameters based on local properties of the superconductor. This framework allows us to model realistic features of superconductor samples, and estimate critical fields as well as energy dissipation under changing fields. Under our framework, TDGL serves as a link between experimental material characterizations and *ab initio* calculations of material-specific parameters, allowing us to further connect these microscopic characterizations with macroscopic SRF performance metrics in a sample-specific way.

The accelerator physics community is large and active, and many studies are highly multidisciplinary. The method presented in this work boasts the advantage of leveraging the expertise of accelerator physicists and engineers, materials scientists, and condensed matter theorists to make sample-specific predictions about realistic SRF materials.

This paper is organized as follows: In section II, we discuss the TDGL equations and show how to calculate TDGL parameters from material properties. We then outline how the spatial variation of the TDGL parameters properties is estimated, combining the results of DFT calculations with experimental material characterizations. We briefly outline the equation formulation we use to solve TDGL with a finite element method. We end the section by showing how dissipation can be calculated from TDGL solutions and deriving how SRF cavity quality factors can be calculated based on this dissipation. In section III we demonstrate our framework by first applying the quality factor estimates to a defect-free Nb simulation. We then estimate critical fields and dissipation for Sn-deficient islands in Nb<sub>3</sub>Sn, comparing

the estimated quality factor of Nb<sub>3</sub>Sn coated SRF cavities with different surface densities of Sn deficient islands. Finally, in section IV, we conclude the paper, justifying the use of TDGL given its known limitations, and discuss the implications of our method and results for future SRF cavity research.

## II. METHODS

### A. The Time-Dependent Ginzburg-Landau Equations

Ginzburg-Landau (GL) theory is one of the oldest theories of superconductivity, and it remains relevant to

day owing to its relative simplicity and direct physical insights into the electrodynamic response of superconductors under static applied fields and currents [52]. The *time-dependent* Ginzburg-Landau (TDGL) equations were originally proposed by Schmid [53] in 1966 and Gor'kov and Eliashberg [54] derived them rigorously from BCS theory later in 1968. The TDGL equations (in Gaussian units) are given by:

$$\Gamma \left( \frac{\partial \psi}{\partial t} + \frac{ie_s \phi}{\hbar} \psi \right) + \frac{1}{2m_s} \left( -i\hbar \nabla - \frac{e_s}{c} \mathbf{A} \right)^2 \psi + \alpha \psi + \beta |\psi|^2 \psi = 0 \quad (1)$$

$$\frac{4\pi\sigma_n}{c} \left( \frac{1}{c} \frac{\partial \mathbf{A}}{\partial t} + \nabla \phi \right) + \nabla \times \nabla \times \mathbf{A} - \frac{2\pi ie_s \hbar}{m_s c} (\psi^* \nabla \psi - \psi \nabla \psi^*) + \frac{4\pi e_s^2}{m_s c^2} |\psi|^2 \mathbf{A} = 0. \quad (2)$$

These equations are solved for the complex superconducting order parameter,  $\psi$ , and the magnetic vector potential,  $\mathbf{A}$ . The magnitude squared of  $\psi$  is proportional to the density of superconducting electrons. The parameters  $\alpha$  and  $\beta$  are phenomenological, and were originally introduced as coefficients of the series expansion of the Ginzburg-Landau free energy. Additionally,  $\phi$  is the scalar potential;  $\sigma_n$  is the normal electron conductivity;  $\Gamma$  is the phenomenological relaxation rate of  $\psi$ . Furthermore,  $e_s = 2e$  and  $m_s = 2m_e$  represent the total charge and total effective mass of a Cooper pair, respectively. The TDGL equations are subject to boundary conditions

$$\left( i\hbar \nabla \psi + \frac{e_s}{c} \mathbf{A} \psi \right) \cdot \mathbf{n} = 0 \quad (3)$$

$$(\nabla \times \mathbf{A}) \times \mathbf{n} = \mathbf{H}_a \times \mathbf{n} \quad (4)$$

$$\left( \nabla \phi + \frac{1}{c} \frac{\partial \mathbf{A}}{\partial t} \right) \cdot \mathbf{n} = 0, \quad (5)$$

where  $\mathbf{n}$  is the outward normal vector to the boundary surface and  $\mathbf{H}_a$  is the applied magnetic field. Eq. 3 ensures no current flows out of the superconducting domain, and noting that  $E = -\nabla \phi - \frac{1}{c} \frac{\partial \mathbf{A}}{\partial t}$ , Eqs. 4 and 5 are electromagnetic interface conditions with an applied magnetic field.

The parameters  $\alpha$ ,  $\beta$ , and  $\Gamma$  were originally introduced into the theory as phenomenological, temperature-dependent constants [55]. It is worth noting that  $\alpha < 0$  corresponds to the superconducting state whereas  $\alpha \geq 0$  corresponds to the normal state;  $\beta$  is strictly positive regardless of the system's state. The TDGL equations can also be derived from microscopic theory using the time-dependent Gor'Kov equations [54]. A useful consequence

of this derivation is that it allows the TDGL parameters to be directly related to experimentally observable properties of the material in question. The material dependencies are given by Ref. 56:

$$\alpha(\nu(0), T_c, T) = -\nu(0) \left( \frac{1 - \frac{T^2}{T_c^2}}{1 + \frac{T^2}{T_c^2}} \right) \quad (6)$$

$$\approx -\nu(0) \left( 1 - \frac{T}{T_c} \right)$$

$$\beta(\nu(0), T_c, T) = \frac{7\zeta(3)\nu(0)}{8\pi^2 T_c^2} \left( \frac{1}{1 + \frac{T^2}{T_c^2}} \right)^2 \quad (7)$$

$$\approx \frac{7\zeta(3)\nu(0)}{8\pi^2 T_c^2}$$

$$\Gamma(\nu(0), T_c) = \frac{\nu(0)\pi\hbar}{8T_c}, \quad (8)$$

where  $\nu(0)$  is the density of states at the Fermi-level,  $T_c$  is the critical temperature,  $T$  is the temperature, and  $\zeta(x)$  is the Riemann zeta function.

A major contribution of this paper is to introduce a framework for modeling sample-specific features of superconducting materials by connecting *ab initio* calculations of the material's properties to experimental characterizations of the material. Eqs. 6-8 determine how the parameters of TDGL depend on the underlying material properties. We allow these parameters to vary spatially to capture the sample-specific features observed from experimental characterizations.

Additionally, when solving the TDGL equations numerically, it is standard to normalize all the parameters

of the model in order to obtain dimensionless quantities. In order to satisfy the above requirements, the steps are as follows: Pick a reference value for each of  $\alpha$ ,  $\beta$ ,  $\Gamma$ , and  $\sigma_n$ , these will most often just be the corresponding values for the bulk material. Label these reference values  $\alpha_0$ ,  $\beta_0$ ,  $\Gamma_0$ , and  $\sigma_{n0}$ . Define dimensionless spatially varying functions,  $a(\mathbf{r})$ ,  $b(\mathbf{r})$ ,  $\gamma(\mathbf{r})$ , and  $s(\mathbf{r})$ , relative to their reference values. Apply the following transformations to Eqs. 1 and 2:

$$\alpha \longrightarrow \alpha_0 a(\mathbf{r}) \quad (9)$$

$$\beta \longrightarrow \beta_0 b(\mathbf{r}) \quad (10)$$

$$\Gamma \longrightarrow \Gamma_0 \gamma(\mathbf{r}) \quad (11)$$

$$\sigma_n \longrightarrow \sigma_{n0} s(\mathbf{r}). \quad (12)$$

Then proceed with standard nondimensionalization procedures for TDGL (see the Appendix for more details). The advantage of this approach is that the nondimensionalization procedures, when used on these transformed equations, leave behind only the dimensionless functions which capture the spatial variation of the sample material in natural units. The resulting equations are

$$\gamma \left( \frac{\partial \psi}{\partial t} + i\kappa_0 \phi \psi \right) + \left( \frac{-i}{\kappa_0} \nabla - \mathbf{A} \right)^2 \psi - a\psi + b|\psi|^2 \psi = 0 \quad (13)$$

$$\frac{s}{u_0} \left( \frac{\partial \mathbf{A}}{\partial t} + \nabla \phi \right) + \nabla \times \nabla \times \mathbf{A} + \frac{i}{2\kappa_0} (\psi^* \nabla \psi - \psi \nabla \psi^*) + |\psi|^2 \mathbf{A} = 0, \quad (14)$$

where  $\kappa_0 = \frac{\lambda_0}{\xi_0}$  is the Ginzburg-Landau parameter of the reference material. The quantity  $\lambda_0 = \sqrt{\frac{m_s c^2 \beta_0}{4\pi e_s^2 |\alpha_0|}}$  is the penetration depth of the reference material, and  $\xi_0 = \sqrt{\frac{\hbar^2}{2m_s |\alpha_0|}}$  is its coherence length. The parameter  $u_0 = \frac{\tau_{\psi_0}}{\tau_{j_0}}$  is a ratio of characteristic time scales in the reference material, where  $\tau_{\psi_0} = \frac{\Gamma_0}{|\alpha_0|}$  is the characteristic relaxation time of  $\psi$  in the reference material and  $\tau_{j_0} = \frac{\sigma_{n0} m_s \beta_0}{e_s^2 |\alpha_0|}$  is the characteristic relaxation time of the current. We have also inserted a minus in front of  $a$ , which is just a convention to make positive values of  $a$  correspond to the superconducting state (Note: this is the opposite of how  $\alpha$  is usually interpreted within Ginzburg-Landau theory, however it is standard to make this change when performing nondimensionalization). The boundary conditions become:

$$\left( \frac{i}{\kappa_0} \nabla \psi + \mathbf{A} \psi \right) \cdot \mathbf{n} = 0 \quad (15)$$

$$(\nabla \times \mathbf{A}) \times \mathbf{n} = \mathbf{H}_a \times \mathbf{n} \quad (16)$$

$$\left( \nabla \phi + \frac{\partial \mathbf{A}}{\partial t} \right) \cdot \mathbf{n} = 0. \quad (17)$$

It should be noted that  $\gamma(\mathbf{r})$  and  $s(\mathbf{r})$  allow the local characteristic time relaxations to vary, which only affects the dynamics of the solutions. Where the time dynamics are relevant these parameters cannot be ignored; however, in many cases, the primary interest of TDGL calculations is in determining the energetic stability and critical fields, such as the superheating field. In these cases, the time dynamics are not relevant and  $\gamma$  and  $s$  can be safely set

to arbitrary constant values, such as unity.

## B. Determining Spatial Variation of TDGL Parameters

In the previous section, we have shown how to introduce spatial variation to the TDGL parameters. The process of calculating the values of  $a(\mathbf{r})$ ,  $b(\mathbf{r})$ , and  $\gamma(\mathbf{r})$  is where we bring in experiment and *ab initio* theory. From Eqs. 6-8, we know these parameters depend on well-defined microscopic quantities, namely  $\nu(0)$  and  $T_c$ . These quantities can be calculated using density-functional theory (DFT). Local densities of states are straightforward to compute in DFT, providing local values for  $\nu(0)$  and superconducting quantities such as  $T_c$  are calculated by applying Eliashberg theory within a DFT framework and directly calculating electron-phonon coupling from first principles. Experiment can then give information about the compositions of sample materials, and DFT calculations can determine the  $\nu(0)$  and  $T_c$  associated with these compositions. Using these values,  $a(\mathbf{r})$ ,  $b(\mathbf{r})$ , and  $\gamma(\mathbf{r})$  are calculated from Eqs. 6-8, and the material geometries from the experimental results determine the spatial variation.

In this paper, we will demonstrate our framework on Sn-deficient islands. These defects have been studied extensively [35, 36, 40, 41] so it is straightforward to find estimates of the general size of these islands and their material compositions in the literature. DFT has also been used to calculate  $\nu(0)$  and  $T_c$  for Nb-Sn systems of different concentrations. In this paper we use a com-

monly observed Sn concentration of 18% and take the DFT values from Ref. 46 to construct  $a(\mathbf{r})$ ,  $b(\mathbf{r})$ , and  $\gamma(\mathbf{r})$ . This paper will primarily focus on the results of our TDGL calculations, for further information regarding the details and results from the DFT calculations used in this paper, we refer the interested reader to Refs. 45 and 46.

### C. Finite Element Formulation

In this paper we solve the TDGL equations in 3D via a finite element method proposed by Gao [57]. We choose the popular temporal gauge which sets the scalar potential  $\phi = 0$  (see Du [58] for a more detailed overview of gauge choices for TDGL). Taking the curl of Eq. 14 allows us to directly solve for the magnetic field and we get a system of 3 equations for  $\psi$ ,  $\mathbf{A}$ , and  $\mathbf{H}$ :

$$\frac{\partial\psi}{\partial t} + \left(\frac{i}{\kappa_0}\nabla + \mathbf{A}\right)^2 \psi - a\psi + b|\psi|^2\psi = 0 \quad (18)$$

$$\frac{1}{u_0}\frac{\partial\mathbf{A}}{\partial t} + \nabla \times \mathbf{H} + \frac{i}{2\kappa_0}(\psi^*\nabla\psi - \psi\nabla\psi^*) + |\psi|^2\mathbf{A} = 0 \quad (19)$$

$$\frac{1}{u_0}\frac{\partial\mathbf{H}}{\partial t} + \nabla \times \nabla \times \mathbf{H} + \frac{i}{\kappa_0}\nabla\psi^* \times \nabla\psi + |\psi|^2\mathbf{H} + \nabla|\psi|^2 \times \mathbf{A} = 0. \quad (20)$$

These equations are subject to the boundary conditions:

$$\left(\frac{i}{\kappa_0}\nabla\psi + \mathbf{A}\psi\right) \cdot \mathbf{n} = 0 \quad (21)$$

$$\mathbf{H} \times \mathbf{n} = \mathbf{H}_a \times \mathbf{n}, \quad (22)$$

where  $\mathbf{n}$  is still the outward normal unit vector and  $\mathbf{H}_a$  is the applied field. We are then able to solve the system by discretizing the test and trial functions with Lagrange finite elements, and using a backward difference scheme for the time derivatives. All computations in this paper were done using the open source software FEniCS [59].

### D. Dissipation in TDGL

When simulating SRF materials, dissipation is often a physical quantity of interest. Under TDGL, a formula for dissipation can be derived by considering the time derivative of the free energy and the free energy current flux density. A more detailed derivation is found in Ref. 56, but we quote the final result here:

$$D = 2\Gamma \left| \left( \frac{\partial\psi}{\partial t} + \frac{ie_s\phi\psi}{\hbar} \right) \right|^2 + \sigma_n \mathbf{E}^2. \quad (23)$$

This quantity is a power density, with the first term corresponding to the superconducting dissipation arising from the relaxation of the order parameter. The second term is the dissipation of normal currents which are largest near the surface where magnetic field can still appreciably penetrate.

It is worth considering how this expression for the dissipation density is related to existing theories of RF power loss and surface resistance. The first term in Eq. 23 is associated with the dissipation due to the rate of change

of  $\psi$ . This term is typically small, except in the vortex state where it becomes the dominant source of dissipation. A dissipation of this form is similar to that proposed by Tinkham [60], who suggested the vortex dissipation should be proportional to  $\left(\frac{\partial\psi}{\partial t}\right)^2$ . The additional term within the parenthesis in Eq. 23 is a result of the gauge invariance of TDGL.

The second term in Eq. 23 can be directly related to the phenomenological ‘‘two-fluid model,’’ which was first proposed by Gorter and Casimir [61] in 1934 and was applied by London [62] later that year to calculate the power loss of a superconductor. The two-fluid model approximates the electrons of the system as consisting of two non-interacting ‘fluids’: the superconducting electrons, in the form of cooper pairs which carry lossless supercurrent, and the normal electrons, which exist as thermally excited quasiparticles that produce typical dissipative currents. Under the two-fluid model, the normal fluid losses produce dissipation of the form [63, 64]

$$P \propto \sigma_n E^2,$$

which is identical to the second term of Eq. 23. For AC applied currents, the electric field is proportional to the frequency and magnetic field,  $E \propto \omega H$ , meaning that overall the power loss will be of the form

$$P \sim \omega^2 H^2. \quad (24)$$

It is also well known that within RF cavities, the power loss is given by

$$P = \frac{1}{2} \oint_A R_s |H(r)|^2 dA, \quad (25)$$

where  $R_s$  is the surface resistance of the cavity walls and  $A$  is the surface area. Comparing Eqs. 24 and 25, we

have that the second term of Eq. 23 directly leads to a surface resistance proportional to the square of the frequency,  $R_s \propto \omega^2$ . In the late 1950s, Mattis and Bardeen [65] as well as Abrikosov, Gor'Kov, and Khalatnikov [66] independently derived the now well-known ‘‘BCS resistance.’’ Under the low frequency and low field limit, the BCS resistance reduces to the form [67, 68]

$$R_{bcs} \simeq \frac{\omega^2}{T} e^{\frac{-\Delta}{k_B T}} \quad (26)$$

where  $\Delta = 1.76k_B T_c$  is the superconducting energy gap [56]. We thus see that our calculated expression for the surface resistance is in good agreement with the  $\omega^2$  dependence of the BCS prediction in the low frequency and field limit.

### E. Estimating Cavity Quality Factor

One of the most important quantities that can be directly estimated from the dissipation is the cavity quality factor,  $Q$ . Quality factor is given by

$$Q = \frac{2\pi E}{\Delta E}, \quad (27)$$

where  $E$  is the energy stored in the cavity and  $\Delta E$  is the energy dissipated in the cavity walls each RF period. These quantities (working in SI units for this section) can be expressed as integrals:

$$E = \frac{1}{2}\mu_0 \int_V dV \mathbf{H}^2 \quad (28)$$

$$\Delta E = \int_0^T dt \int_{V_{surf}} dV_{surf} D, \quad (29)$$

where  $V$  is the cavity volume,  $T$  is the RF period, and  $D$  is given by Equation 23.  $V_{surf}$  is the volume in the first few penetration depths of the cavity surface where essentially all of the dissipation occurs. TDGL simulation outputs are unit-free, so it is helpful to pull constants with units out of these integrals, leaving behind dimensionless functions which can be calculated from TDGL solutions. We start by expressing Equation 28 in cylindrical coordinates:

$$E = \frac{1}{2}\mu_0 \int r dr \int d\phi \int dz \mathbf{H}^2$$

We then define some dimensionless quantities:

$$\tilde{r} = \frac{r}{R} \quad (30)$$

$$\tilde{z} = \frac{z}{L} \quad (31)$$

$$\tilde{\mathbf{H}} = \frac{\mathbf{H}}{H_a} \quad (32)$$

Where  $R$  is the maximum radius of the cavity,  $L$  is the length of the cavity in the axial direction, and  $H_a$  is the

maximum value of the applied field at the surface of the cavity during an RF period. These quantities allow the definition of a unit-less integral that only depends on the cavity geometry:

$$I_H \equiv \int \tilde{r} d\tilde{r} \int d\tilde{z} \tilde{\mathbf{H}}^2 \quad (33)$$

Using these definitions with Equation 28 and assuming that  $\mathbf{H}$  has azimuthal symmetry results in

$$E = \pi\mu_0 H_a^2 L R^2 I_H. \quad (34)$$

Turning to the dissipated energy integral, suppose all of the dissipation occurs within a distance  $d$  below the cavity surface, where  $d \ll R$ . This allows the cylindrical integral to be converted into cartesian coordinates, with the azimuthal direction becoming the new  $x$  direction, the axial direction becoming the new  $y$  direction, and the radial direction becoming the new  $z$  direction. Doing this, we have

$$\Delta E = \int_0^T dt \int_0^{2\pi R} dx \int_0^L dy \int_0^d dz D. \quad (35)$$

When calculating this from simulation outputs, the integral is necessarily calculated over a small region of the overall cavity surface. Let  $L_x$  and  $L_y$  be the simulation domain size in the  $x$  and  $y$  directions respectively, and let  $N$  be the total number of simulation areas needed to fully partition the cavity surface. Then the dissipation integral becomes

$$\Delta E = N \int_0^T dt \int_0^{L_x} dx \int_0^{L_y} dy \int_0^d dz D, \quad (36)$$

and  $N$  can be approximated as

$$N = \frac{2\pi RL}{L_x L_y}. \quad (37)$$

Continuing as before we again define dimensionless coordinates:

$$\tilde{x} = \frac{x}{\lambda} \quad (38)$$

$$\tilde{y} = \frac{y}{\lambda} \quad (39)$$

$$\tilde{z} = \frac{z}{\lambda} \quad (40)$$

$$\tilde{t} = \frac{T_{sim} t}{T} \quad (41)$$

where  $\lambda$  is the penetration depth and  $T_{sim}$  is the period in units of simulation time. These convert the integral to

$$\Delta E = \lambda^3 \frac{T}{T_{sim}} N \int_0^{T_{sim}} d\tilde{t} \int_0^{\frac{L_x}{\lambda}} d\tilde{x} \int_0^{\frac{L_y}{\lambda}} d\tilde{y} \int_0^{\frac{d}{\lambda}} d\tilde{z} D. \quad (42)$$

Additionally, under the temporal gauge ( $\phi = 0$ ), Equation 23 can be expressed as

$$D = 2\mu_0 H_c^2 \frac{T_{sim}}{T} \left( \left| \frac{\partial \tilde{\psi}}{\partial \tilde{t}} \right|^2 + \sigma_n \mu_0 \lambda^2 \frac{T_{sim}}{T} \left( \frac{\partial \tilde{\mathbf{A}}}{\partial \tilde{t}} \right)^2 \right), \quad (43)$$

where  $\tilde{\psi}$  and  $\tilde{\mathbf{A}}$  are the unit-free versions of the vector potential and order parameter that are solved for with Eqs. 13 and 14 (a derivation of Equation 43 can be found in the Appendix). Finally, we define some more dimensionless integrals over the TDGL solutions:

$$I_\psi \equiv \int_0^{T_{sim}} dt \int_0^{\frac{L_x}{\lambda}} d\tilde{x} \int_0^{\frac{L_y}{\lambda}} d\tilde{y} \int_0^{\frac{d}{\lambda}} d\tilde{z} \left| \frac{\partial \tilde{\psi}}{\partial \tau} \right|^2 \quad (44)$$

$$I_A \equiv \int_0^{T_{sim}} dt \int_0^{\frac{L_x}{\lambda}} d\tilde{x} \int_0^{\frac{L_y}{\lambda}} d\tilde{y} \int_0^{\frac{d}{\lambda}} d\tilde{z} \left( \frac{\partial \tilde{\mathbf{A}}}{\partial \tau} \right)^2 \quad (45)$$

Combining everything and noting that  $\omega = \frac{2\pi}{T}$ , we get

$$\Delta E = 2\mu_0 H_c^2 \lambda^3 \frac{2\pi RL}{L_x L_y} \left( I_\psi + \omega \frac{\sigma_n \mu_0 \lambda^2 T_{sim}}{2\pi} I_A \right). \quad (46)$$

Now using Equations 27, 34, and 46 we get an expression for the quality factor,

$$Q = \frac{\tilde{H}_a^2 RL_x L_y I_H}{2\lambda^3 \left( I_\psi + \omega \frac{\sigma_n \mu_0 \lambda^2 T_{sim}}{2\pi} I_A \right)}, \quad (47)$$

where  $\tilde{H}_a \equiv \frac{H_a}{\sqrt{2}H_c}$  is the applied field in simulation units. It is common to express the quality factor as

$$Q = \frac{G}{R_s}, \quad (48)$$

where  $R_s$  is the cavity surface resistance and  $G$  is a geometric factor that depends only on quantities which are determined by the cavity geometry. We can define these quantities under the framework we have presented as

$$G = \frac{1}{2} \mu_0 \omega R I_H \quad (49)$$

$$R_s = \frac{\mu_0 \omega \lambda^3}{\tilde{H}_a^2 L_x L_y} \left( I_\psi + \omega \frac{\sigma_n \mu_0 \lambda^2 T_{sim}}{2\pi} I_A \right). \quad (50)$$

For a typical 1.3 GHz 9-cell Nb TESLA cavity,  $G = 270 \Omega$  [69], so in practice we can just use this value or other known values of  $G$ , and only calculate  $R_s$  from Equation 50.

The  $\sigma_n$  in the above equations is the conductivity of only the normal electrons. A simple way to estimate this value is to consider the Drude model conductivity [70],

$$\sigma = \frac{ne^2\tau}{m}, \quad (51)$$

where  $e$  and  $m$  are the electron charge and mass,  $n$  is the number density of electrons, and  $\tau$  is their mean free collision time. In the superconducting state, we can make the usual assumption from the two-fluid model that  $n = n_s + n_n$  where  $n_s$  and  $n_n$  are the number densities of the superconducting and normal electrons respectively. Under TDGL,  $n_s = \frac{\alpha}{\beta} |\tilde{\psi}|^2$  and so the normal conductivity is

$$n_n = n - \frac{\alpha}{\beta} |\tilde{\psi}|^2. \quad (52)$$

Using this along with Equation 51, the normal electron conductivity in the Meissner state can be estimated with

$$\sigma_n = \frac{ne^2\tau}{m} \left( 1 - \frac{1}{n} \frac{\alpha}{\beta} |\tilde{\psi}|^2 \right). \quad (53)$$

In the above calculations, it was assumed that the cavity surface is partitioned into small fractional areas, and the dissipated energy is calculated over one of these areas, and then multiplied by the total number of them. If some defect was present in the simulation domain, it would mean that a  $Q$  calculation based purely on that value would be assuming that such a defect is uniformly distributed over the surface of the domain. In Equation 50, the only thing that changes when simulating a different material or different defect is the value of the quantity in parenthesis, every other part of the process for calculating  $Q$  remains the same. This means that we can calculate a more realistic cavity surface resistance by calculating the  $R_s$  with Equation 50 for a few different simulations, and then taking a weighted average of these values. Let  $R_i$  be the surface resistance of the  $i$ th simulation, and let  $p_i$  be the percentage of the fractional areas partitioning the cavity surface which are represented by this simulation. Then

$$R_{tot} = \sum_i p_i R_i, \quad (54)$$

where  $\sum_i p_i = 1$ . The simplest application for Equation 54 is to perform two simulations, one baseline simulation with no defects or material inhomogeneity, and then another simulation containing some defect of interest. Choosing a value  $p$  to represent the percentage of fractional areas containing the defect and then following through with the rest of the quality factor calculation provides a simple way to estimate  $Q$  for different average defect densities by simply changing the value of  $p$ .

The value of  $Q$  calculated from TDGL outputs will typically be underestimated at low field. This is because of the assumption of gapless superconductivity, which results in higher surface resistances than is predicted with the BCS surface resistance (Equation 26). Despite this, our approach still often predicts quality factors within an order of magnitude of the experimental values. Additionally, the relative behavior of  $Q$  at different applied fields, especially when averaging the impact of multiple kinds of defects as described above, qualitatively captures effects such as high field  $Q$ -slope.

### III. VALIDATION STUDY

We now demonstrate the use of the methods from Section II. The geometry used within the simulations in this section is depicted in Fig. 1. The domains used are rectangular cuboids, with periodic boundary conditions in the  $x$  and  $y$  directions, denoted by the yellow and light blue highlights, respectively. The external field is applied

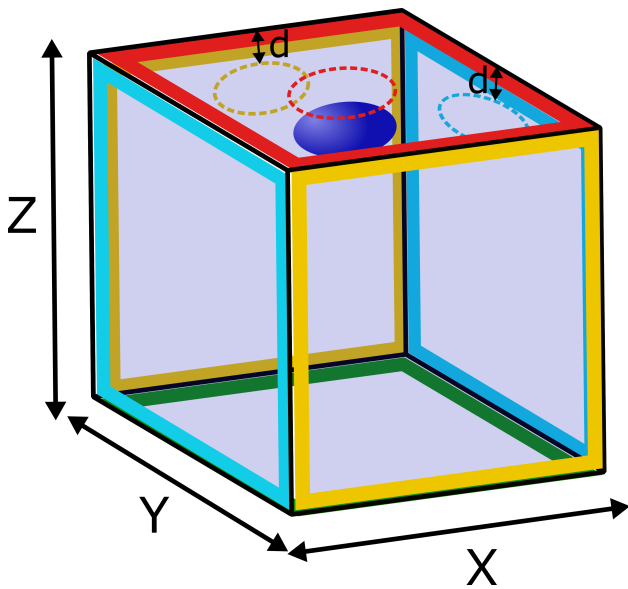


FIG. 1: **A Schematic of our Simulation Geometry.**

Like-colored surfaces (The surfaces outlined in yellow and light blue) have periodic boundary conditions. The red and green outlined surfaces are where field is applied, which can be different on each surface. Often, the red surface is where we will apply the field, with no field applied on the green surface. The Sn-deficient island is depicted as a dark blue ellipsoid, with dotted lines showing the projection of the ellipsoid into the XZ, XY, and YZ planes, the color of the ellipse corresponds to the face it is projected into. The island's distance from the surface is measured from the surface to the outer edge of the ellipsoid, denoted by  $d$ .

on the upper and lower surfaces in the  $z$  direction, highlighted in red and green in the figure. For the simulations in this paper, we apply the field just on the red surface, with no field applied to the green surface. For simulations including Sn-deficient islands, such an island is also depicted in Fig. 1 (the dotted ellipses show the projection of the ellipsoid into each surface). For the Sn-deficient island simulations in this paper, we choose the ellipsoids to have equal  $x$  and  $y$  radii and a  $z$  radius of half the  $x$  radius. The island's distance from the surface, denoted on the figure by  $d$ , is measured from the surface to the outer edge of the ellipsoid. All of our simulations were solved using cubic meshes with tetrahedral elements, all generated using the open source mesh generation program, Gmsh [71]. For the Sn-deficient island simulations, the OpenCASCADE geometry kernel available within Gmsh was used to make the mesh conform to the shape of the islands.

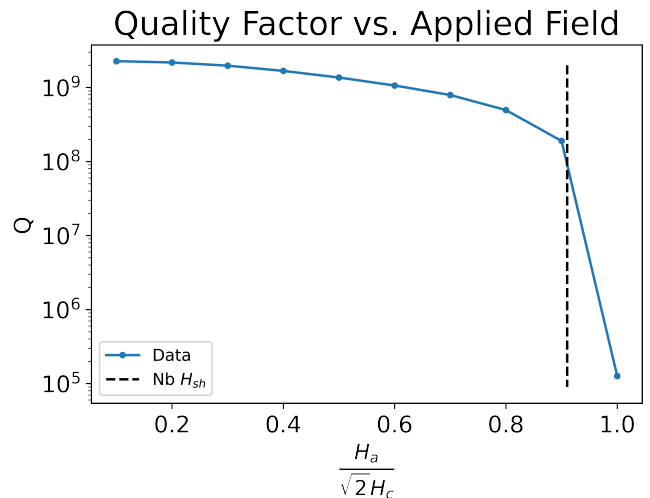


FIG. 2: **Nb SRF Cavity Quality Factor vs. Applied Field.** A plot of quality factor for a uniform Nb simulation versus the applied field (in units of  $\sqrt{2}H_c$ ). The quality factor is calculated using Eqs. 48 and 50 with  $G = 270 \Omega$ . The dotted black line indicates the superheating field of Nb. Because it is above  $H_{sh}$ , vortex nucleation occurred for  $\bar{H}_a = 1.0$  which is the reason for the sharp drop in  $Q$ .

#### A. Nb SRF Cavity Quality Factors

We start by demonstrating the calculation of quality factor using Eqs. 48 and 50. We simulate a 1.3 GHz Nb cavity ( $G = 270 \Omega$ ), which typically have quality factors in the range of  $10^{10} - 10^{11}$ . Our simulation domain for these simulations is a cube with side length  $20\lambda$  and we use a sinusoidal applied field with a period of  $2000\tau_\psi$ . Since  $\tau_\psi = \frac{\Gamma}{\alpha}$ , we can use Eqs. 6 and 8, and  $\nu(0) = 90$  states/(eV nm<sup>3</sup>) (value obtain from private correspondence) to get that for Nb at 2K,  $\tau_\psi = 3.7 \times 10^{-13}$  s. As a result, a period of  $2000\tau_\psi$  corresponds to a frequency of  $\sim 1.3$  GHz. Our results for this simulation are shown in Figure 2. We see that the low field quality factor is  $\sim 2 \times 10^9$ , this is only a little below the expected range of  $10^{10} - 10^{11}$ , which can be easily explained by the assumption of gapless superconductivity under TDGL, which causes  $Q$  to be underestimated. There is a sharp drop in  $Q$  once the applied field crosses the superheating field of niobium (the black dotted line) and vortices start to nucleate.

We can also plot the unitless dissipation values that are used to calculate  $Q$ . Figure 3 depicts the dissipation values for the two terms in parentheses in Equation 46. We find that, as expected, the term due to the dissipation of the electric field ( $\frac{\sigma_n \mu_0 \lambda^2}{\tau_\psi} I_A$ ) is larger than the term due to order parameter relaxation ( $I_\psi$ ) by about two orders of magnitude. The  $I_\psi$  term grows faster than the  $I_A$  term and the two are equal at an applied field of  $\frac{H_a}{\sqrt{2}H_c} =$



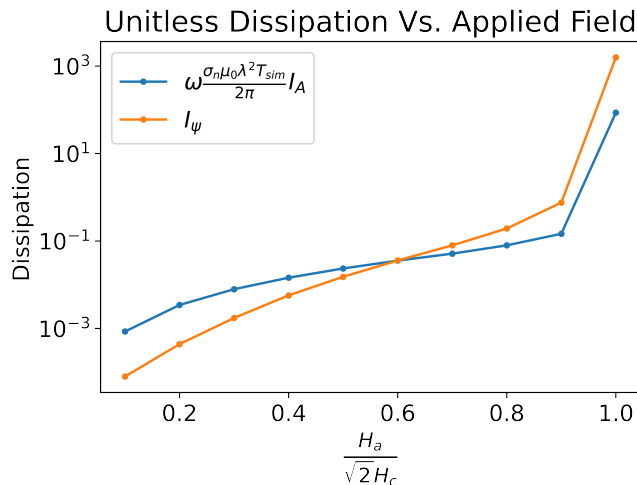


FIG. 3: **Comparison of Different Dissipation Terms.** The values of the two terms in parentheses in Equation 46 are plotted separately. We see that the (unit-free) dissipation of the electric field ( $\omega \frac{\sigma_n \mu_0 \lambda^2 T_{sim}}{2\pi} I_A$ ) is two orders of magnitude larger than the corresponding dissipation from the order parameter relaxation ( $I_\psi$ ). The  $I_\psi$  term grows faster with field, and the two terms are equal at an applied field of 0.6, above which the  $I_\psi$  term dominates, and grows even faster once vortices nucleate above the superheating field.

0.6, and at higher fields, the  $I_\psi$  term remains dominant, particularly above the superheating field where it grows much faster due to vortex nucleation and motion. These results demonstrate how the methods in this paper can be used to calculate the dissipation for ideal cases like uniform niobium. We will use them again for the case of Sn-deficient islands in Section III B.

### B. Sn-deficient Islands in Nb<sub>3</sub>Sn

There has been a considerable amount of work both experimentally and theoretically understanding the various defects present in Nb<sub>3</sub>Sn [19, 34–41]. For the purposes of this paper, we will focus on Sn-deficient islands, small regions within Nb<sub>3</sub>Sn grains that have lower than expected Sn concentrations. To demonstrate the use of our sample specific TDGL framework, we will estimate the potential impact to SRF performance by determining the vortex penetration field,  $H_{vort}$ . This field is the lowest field at which a vortex nucleates, it is a generalization of the superheating field for surfaces containing defects, and it is equal to the superheating field in the limit of a completely uniform flat surface.

In order to simulate Sn-deficient islands, we need estimates of the properties of the material within these regions. We choose a Sn concentration of 18 at.% for our islands. Using this value as well as DFT calculations

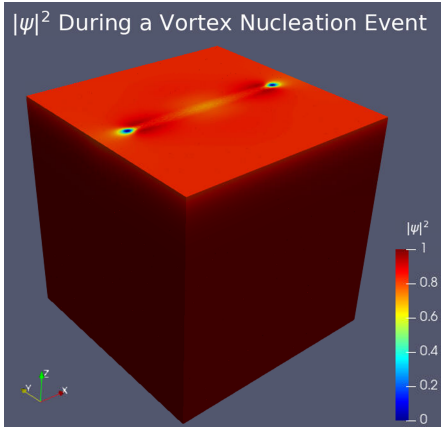
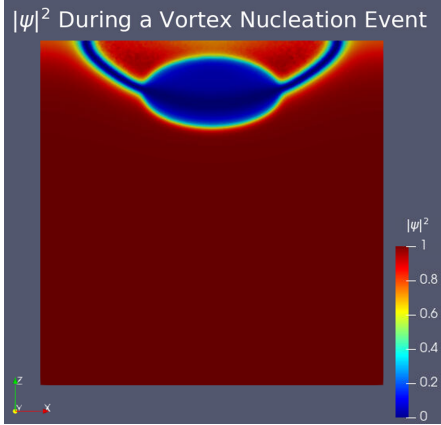
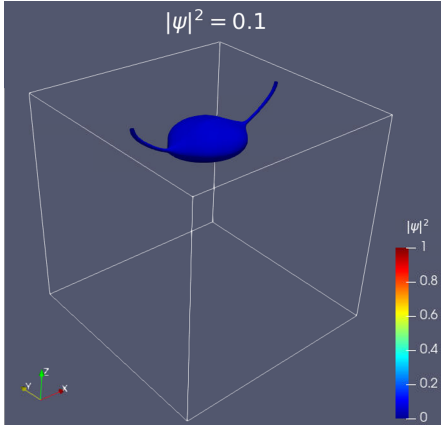
TDGL Parameter and Material Values		
Quantity	Bulk Value	Island Value
$T_c$ (K)	18	6
$\nu(0)$ (states/(eV*nm <sup>3</sup> ))	101.33	40.53
$a$ (unitless)	1	0.15
$b$ (unitless)	1	1.8
$\gamma$ (unitless)	1	1.2
$s$ (unitless)	1	1

TABLE I: **A summary of the TDGL parameter and material values used in the results of this paper.** All TDGL parameters were calculated from Equations 6-8 using the higher order temperature dependence and normalized with respect to the bulk value. The  $T_c$  and  $\nu(0)$  values were taken from Ref. 46 assuming a Sn concentration of 18% for the island. The normal electron conductivity,  $s$ , was assumed to remain constant throughout the simulation domain.

for Nb<sub>3</sub>Sn from Sitaraman et al. [46], we estimate the critical temperature and density of states. Using these values, we construct  $a(\mathbf{r})$ ,  $b(\mathbf{r})$ , and  $\gamma(\mathbf{r})$ ; the values of these quantities in the bulk as well as in the island are reported in Table I. The simulation geometry is the same as depicted in Fig. 1, with the domain a cube with side length  $10\lambda$ . The applied field for these simulations was a constant value.

Figure 4 depicts vortex nucleation occurring at  $H_{vort}$  for a particular island. We find that varying the distance of the island from the surface between 0.1 and 2 penetration depths (i.e. between  $\sim 10$ -200 nm for Nb<sub>3</sub>Sn), we observe a reduction in  $H_{vort}$  by as much as  $\sim 70\%$  down from the bulk value of the superheating field for islands very near the surface, as shown in Fig. 5. We did this for several different island sizes, and found that the severity of this drop in  $H_{vort}$  increases with increasing island size. As such, we can conclude that large islands within 200 nm of the cavity surface are a potential cause for concern when it comes to SRF performance, particularly ones very close to the surface.

Using these solutions, we can also calculate the dissipation due to the Sn-deficient islands, and estimate their quality factors. To do so, we change our applied field to be sinusoidal with a period of  $1000\tau_{\psi_0}$ , which corresponds to a frequency on the order of  $\sim 5$  GHz. Most Nb<sub>3</sub>Sn cavities use a frequency lower than this, but these simulations already had immense computational cost, so using a  $5\times$  longer period would make them prohibitively expensive. When running TDGL simulations, to get good solution convergence, the mesh elements must be smaller than a coherence length (and ideally much smaller). This means simulating Nb<sub>3</sub>Sn is extremely challenging, as it has  $\kappa = \sim 26$ , meaning the domain both has to be large enough to capture at least a few penetration depths, while also being refined enough to have elements that are a few times smaller than a coherence length. When determining  $H_{vort}$ , the mesh size (and therefore computational

(a) A plot of  $|\psi|^2$  during a vortex nucleation event.(b) A 2D slice of  $|\psi|^2$  in the XZ plane at  $\frac{z}{\lambda} = 5$ (c) The  $|\psi|^2 = 0.1$  isosurface.FIG. 4: **Example of a Sn-deficient Island**

**Simulation.** The domain is a cube with side length  $10\lambda$ , this particular simulation is for an island  $0.5\lambda$  from the surface, with a X and Y radius of  $2\lambda$  and a Z radius of  $1\lambda$ . The applied field is  $\frac{H_a}{\sqrt{2}H_c} = 0.38$ , which is the value of  $H_{vort}$  for this island size and distance from the surface. (a) depicts a volume plot of  $|\psi|^2$  over the whole domain during a vortex nucleation event. (b) is a 2D slice in the XZ plane at  $\frac{z}{\lambda} = 5$ . (c) is the  $|\psi|^2 = 0.1$  isosurface, which shows the shape of the vortex as well as the island that induced the nucleation.

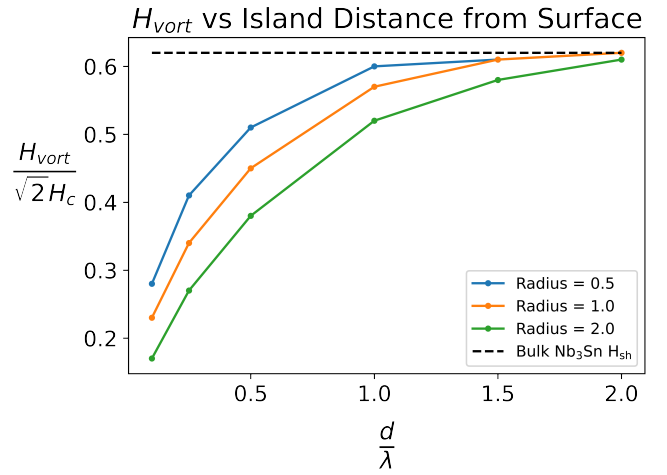


FIG. 5: **Vortex Penetration Field Versus Distance from Surface.** We plot our calculated vortex penetration field estimates, varying the distance of the Sn deficient island from the superconductor surface. The field values are reported in units of  $\sqrt{2}H_c$  and the distances are in units of penetration depths. We did this for 3 different islands, with x radii of 0.5, 1, and 2 penetration depths. The black dotted line denotes the superheating field of bulk  $Nb_3Sn$ . Smaller volume islands have a diminishing impact on  $H_{vort}$ .

cost) can be reduced by only significantly refining the mesh right near the surface, where vortices will nucleate. Once a vortex begins to nucleate, we know that the applied field is above  $H_{vort}$  and thus the rest of that simulation is no longer relevant. However, calculating dissipation requires enough resolution throughout the mesh for a vortex to be able to nucleate, and then move around to dissipate energy, and with a sinusoidal applied field, the vortices can partially nucleate, and then get pushed back out of the superconductor as the field changes. The result of this is that simulations to estimate the dissipation and quality factor of Sn-deficient islands are *much* more computationally expensive than estimating  $H_{vort}$ , and so we will only be simulating the smallest island size at a distance from the surface of  $0.5\lambda$  and we decreased our domain size to a  $5\lambda \times 2.5\lambda \times 2.5\lambda$  rectangular cuboid with the long direction oriented in the same direction as the applied field (and thus the initial orientation of any vortices that nucleate).

Figure 6 shows the results for our quality factors. We ran two simulations, a baseline simulation with no island and a Sn-deficient island with the size described above. Then using Equation 54, we estimated the effective total cavity surface resistance for a number of different island densities. The percentage of island coverage in this figure is calculated by determining the fraction of the total simulation surface area occupied by the island projected into the XY plane and multiplying it by the weighting on the surface resistance from the island simulations used in

Equation 54. the 0% island coverage curve (in blue) is the quality factor calculated only from the simulation without an island, and the 6.3% curve (in pink) is the quality factor calculated only from the simulation with an island. We see that above  $H_{vort}$  for this island size and distance from the surface vortices begin nucleating, with basically all of the deviations between different island coverages happening only above this value. For cavities with  $\geq 1.5\%$  of their surface containing an island, the drop in quality factor starts to become very significant, with even small increases in island density leading to significant drops in quality factor. The noise in the calculations here is largely due to numerical variations in how many vortices enter, and how much they move around. The temperature of the simulation is held constant at the Nb<sub>3</sub>Sn operating temperature of 4.2K, so it is likely that these vortices would realistically lead to heating and subsequent cavity quench once the field is much higher than  $H_{vort}$ . The low field magnitude of the quality factor in these simulations is  $\sim 10^8$ . This is lower than the expected value of  $\sim 10^{10}$ , partly because of being at a higher frequency than 1.3 GHz, and also because the embedded assumption of gapless superconductivity in TDGL means that it will typically underestimate  $Q$  (as discussed in Section IIE). Given infinite computational time (or a lower  $\kappa$  material), this kind of calculation could be repeated for a variety of island sizes and distances, and applying the defect averaging approach described in Section IIE, the resulting  $Q$  plots would look increasingly like the high field  $Q$  slope plots taken experimentally from real cavities.

#### IV. CONCLUSION

In this paper we have presented a method which allows time-dependent Ginzburg-Landau to serve as a mesoscopic link between microscopic experimental measurements and *ab initio* calculations with macroscopic SRF performance metrics, such as quality factor and quench fields. By allowing the parameters of TDGL to vary in space, and writing them in terms of well defined local quantities like the Fermi-level density of states and the critical temperature, material profiles can be constructed which allow TDGL to accurately simulate the superconducting and electromagnetic response of realistic material samples. We used this method to model Sn-deficient islands and calculated that there could be up to a 70% reduction in  $H_{sh}$  for islands which are close to the cavity surface. The theoretical maximum accelerating gradient for Nb<sub>3</sub>Sn cavities is around 100 MV/m, but the highest accelerating field achieved so far by a Nb<sub>3</sub>Sn SRF cavity is around 24 MV/m [16], a  $\sim 75\%$  decrease. Since SRF cavity quench fields are directly related to  $H_{sh}$ , our predicted 70% reduction in  $H_{vort}$  is strong evidence that near-surface (within  $\sim 10$ -200 nm) Sn-deficient islands may be one of the contributing factors to poor cavity performance. We further support this evidence

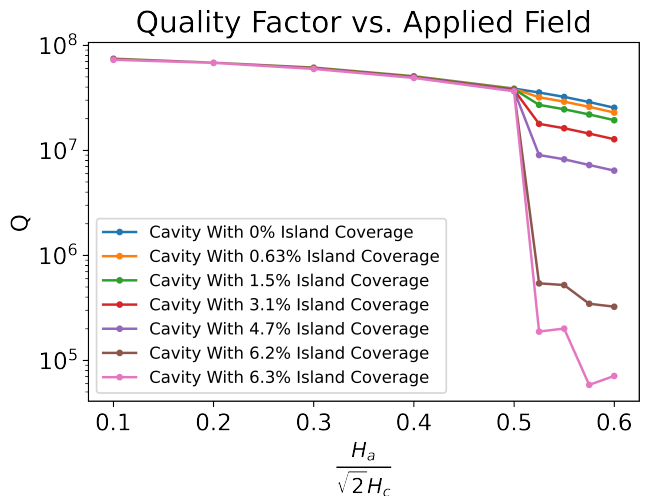


FIG. 6: **Quality Factor for a Sn-deficient Island.**

Quality factor plots using Equation 54 to estimate different densities of Sn-deficient islands by averaging results from simulations both with and without an island. The ellipsoid island has X and Y radii of  $0.5\lambda$  and a Z radius of  $0.25\lambda$ . The top edge of the island is  $0.5\lambda$  below the upper surface. Vortices begin nucleating for the island simulation at an applied field of 0.525.

The percentage of island coverage was calculated by taking the fraction of the total simulation surface area occupied by the island (which for these simulations was  $\sim 6.3\%$ ) and multiplying it by the weighting on the surface resistance from the island simulations used in Equation 54. So the 0% island coverage curve (in blue) is the quality factor calculated only from the simulation without an island, and the 6.3% curve (in pink) is the quality factor calculated only from the simulation with an island.

with calculations of the quality factor due to Sn-deficient islands, finding significant drops in quality factor above  $H_{vort}$ , even for relatively small fractions of the cavity surface area containing islands, and this effect would likely be even more significant in potential future simulation performing the same analysis for larger islands closer to the surface (or even fully exposed) and coupling the dissipation to a temperature field to allow for thermal runaway effects which could simulate cavity quenching.

A recent study performing centrifugal barrel polishing (CBP) on Nb<sub>3</sub>Sn SRF cavities to smooth the RF surface recently found that doing so led to a decrease in the overall quality factor, as well as lower field for the onset of Q-slope and a lower quench field. Performing another Sn vapor deposition recovered the previous quality factor performance, but with a higher quench field [72]. Our results provide strong evidence for the origin of these effects, described as follows: CBP smooths the RF surface, but results in the removal of surface material, exposing previously deep Sn-deficient islands. These near-surface islands lead to increased dissipation, lowering the overall

quality factor. Vortex nucleation induced by the islands at higher fields leads to onset of Q-slope and eventually an early cavity quench. Performing an additional Sn deposition removes the Sn deficiencies to recover the original quality factor, but now reaching higher quench fields due to the smoother surface.

Whenever using the TDGL equations to make predictions about experimental systems, it is important to consider their limitations. They are formally valid for gapless superconductivity, as gapped superconductors have a singularity in their density of states which prevents expansions in powers of the energy gap [73]. Additionally, the equations are only quantitatively valid near the critical temperature. The first of these conditions can be avoided with the use of a generalized version of TDGL first proposed by Kramer and Watts-Tobin [74]. Future work could include the use of this generalized TDGL; however, it should be noted that Proslir et al. [75] observed a broadening in the density of states due to Nb oxides leading to a gapless superconducting surface layer in certain Nb SRF cavities. Gurevich and Kubo [68, 76] later showed that under typical SRF operating conditions and material compositions, there is a generic broadening of the density of states and lowering of the gap, which further justifies the use of TDGL for SRF applications.

The methods for simulating realistic sample-specific material defects and calculating the resulting quality factors presented in this paper represents a promising tool for understanding the impact of many different underlying material features on SRF performance. Many of these features are impossible to probe experimentally, so this method will be useful in assisting the design and manufacturing of the next generation of SRF cavities.

## V. ACKNOWLEDGEMENT

This work was supported by the US National Science Foundation under Award OIA-1549132, the Center for Bright Beams. We would like to thank Dr. Nathan Sitaraman for helpful conversations and estimates of the Fermi level density of states for Nb, and Dr. Michelle Kelley for helpful comments about early drafts of the methods section.

### Appendix: TDGL Non-dimensionalization

To nondimensionalize the TDGL equations, we start with Eqs. 1 and 2, and make the following coordinate

transformations:

$$\begin{aligned}\nabla &\longrightarrow \frac{1}{\lambda_0} \tilde{\nabla} \\ \frac{\partial}{\partial t} &\longrightarrow \frac{1}{\tau_{\psi_0}} \frac{\partial}{\partial \tilde{t}} \\ \mathbf{A} &\longrightarrow \sqrt{2} H_{c0} \lambda_0 \tilde{\mathbf{A}} \\ \psi &\longrightarrow \sqrt{\frac{|\alpha_0|}{\beta_0}} \tilde{\psi} \\ \phi &\longrightarrow \phi_0 \tilde{\phi}.\end{aligned}$$

If we substitute in Eqs. 9, 10, 11, and 12 for  $\alpha$ ,  $\beta$ ,  $\Gamma$ , and  $\sigma_n$  respectively, we can then define the quantities:

$$\begin{aligned}\lambda_0 &= \sqrt{\frac{m_s c^2 \beta_0}{4\pi e_s^2 |\alpha_0|}} \\ \xi_0 &= \sqrt{\frac{\hbar^2}{2m_s |\alpha_0|}} \\ \kappa_0 &= \frac{\lambda_0}{\xi_0} \\ H_{c0} &= \sqrt{\frac{4\pi \alpha_0^2}{\beta_0}} \\ \tau_{\psi_0} &= \frac{\Gamma_0}{|\alpha_0|} \\ \tau_{j_0} &= \frac{\sigma_{n0} m_s \beta_0}{e_s^2 |\alpha_0|} \\ u_0 &= \frac{\tau_{\psi_0}}{\tau_{j_0}} \\ \phi_0 &= \frac{\hbar \kappa_0}{e_s \tau_{\psi_0}}.\end{aligned}$$

Using these relations, the resulting equations under the above coordinate transformations simplify into Eqs. 13 and 14 (where we then drop the tildes).

### Appendix: Nondimensionalizing the TDGL Dissipation

We start with Equation 23,

$$D = 2\Gamma \left| \left( \frac{\partial \psi}{\partial t} + \frac{i e_s \phi \psi}{\hbar} \right) \right|^2 + \sigma_n \mathbf{E}^2$$

choosing the temporal gauge ( $\phi = 0$ ) we have

$$D = 2\Gamma \left| \frac{\partial \psi}{\partial t} \right|^2 + \sigma_n \left( \frac{\partial \mathbf{A}}{\partial t} \right)^2.$$

Next, we make the same coordinate transformations as from the previous section (and the same time transformation as from the methods section) and use the expressions

for  $\tau_\psi$  and  $H_c$  on the first term:

$$\begin{aligned} D &= \frac{2\Gamma\alpha T_{sim}^2}{\beta T^2} \left| \frac{\partial\tilde{\psi}}{\partial\tilde{t}} \right|^2 + 2\sigma_n H_c^2 \lambda^2 \frac{T_{sim}^2}{T^2} \left( \frac{\partial\tilde{\mathbf{A}}}{\partial\tilde{t}} \right)^2 \\ &= \frac{2\tau_\psi\alpha^2 T_{sim}^2}{\beta T^2} \left| \frac{\partial\tilde{\psi}}{\partial\tilde{t}} \right|^2 + 2\sigma_n H_c^2 \lambda^2 \frac{T_{sim}^2}{T^2} \left( \frac{\partial\tilde{\mathbf{A}}}{\partial\tilde{t}} \right)^2 \\ &= \frac{2H_c^2 T_{sim}}{4\pi T} \left| \frac{\partial\tilde{\psi}}{\partial\tilde{t}} \right|^2 + 2\sigma_n H_c^2 \lambda^2 \frac{T_{sim}^2}{T^2} \left( \frac{\partial\tilde{\mathbf{A}}}{\partial\tilde{t}} \right)^2, \end{aligned}$$

where in the last line we used the fact that  $T = \tau_\psi T_{sim}$ . Finally, this expression is in Gaussian units so we con-

vert to SI units so that it is compatible with the other expressions in Section II E:

$$\begin{aligned} D &= 2\tau_\psi\mu_0 H_c^2 \frac{T_{sim}^2}{T^2} \left| \frac{\partial\tilde{\psi}}{\partial\tilde{t}} \right|^2 + 2\sigma_n\mu_0^2 H_c^2 \lambda^2 \frac{T_{sim}^2}{T^2} \left( \frac{\partial\tilde{\mathbf{A}}}{\partial\tilde{t}} \right)^2 \\ &= 2\mu_0 H_c^2 \frac{T_{sim}}{T} \left( \left| \frac{\partial\tilde{\psi}}{\partial\tilde{t}} \right|^2 + \sigma_n\mu_0\lambda^2 \frac{T_{sim}}{T} \left( \frac{\partial\tilde{\mathbf{A}}}{\partial\tilde{t}} \right)^2 \right) \end{aligned}$$

- 
- [1] S. Posen and M. Liepe, Advances in development of nb<sub>3</sub>Sn superconducting radio-frequency cavities, *Phys. Rev. ST Accel. Beams* **17**, 112001 (2014).
- [2] S. Posen and D. L. Hall, nb<sub>3</sub>Sn superconducting radiofrequency cavities: fabrication, results, properties, and prospects, *Superconductor Science and Technology* **30**, 033004 (2017).
- [3] A. Gurevich, Theory of rf superconductivity for resonant cavities, *Superconductor Science and Technology* **30**, 034004 (2017).
- [4] Z. Sun, T. Oseroff, Z. Baraissov, D. K. Dare, K. Howard, B. Francis, A. C. Hire, N. Sitaraman, T. A. Arias, M. K. Transtrum, R. Hennig, M. O. Thompson, D. A. Muller, and M. U. Liepe, Zrnb(co) rf superconducting thin film with high critical temperature in the theoretical limit, *Advanced Electronic Materials* **9**, 2300151 (2023).
- [5] N. S. Sitaraman, Z. Sun, B. L. Francis, A. C. Hire, T. Oseroff, Z. Baraissov, T. A. Arias, R. G. Hennig, M. U. Liepe, D. A. Muller, and M. K. Transtrum (Center for Bright Beams), Enhanced surface superconductivity of niobium by zirconium doping, *Phys. Rev. Appl.* **20**, 014064 (2023).
- [6] J. Bardeen and M. J. Stephen, Theory of the motion of vortices in superconductors, *Phys. Rev.* **140**, A1197 (1965).
- [7] D. B. Liarte, S. Posen, M. K. Transtrum, G. Catelani, M. Liepe, and J. P. Sethna, Theoretical estimates of maximum fields in superconducting resonant radio frequency cavities: stability theory, disorder, and laminates, *Superconductor Science and Technology* **30**, 033002 (2017).
- [8] S. Posen, N. Valles, and M. Liepe, Radio frequency magnetic field limits of nb and nb<sub>3</sub>Sn, *Phys. Rev. Lett.* **115**, 047001 (2015).
- [9] L. Kramer, Stability limits of the meissner state and the mechanism of spontaneous vortex nucleation in superconductors, *Phys. Rev.* **170**, 475 (1968).
- [10] A. J. Dolgert, S. J. Di Bartolo, and A. T. Dorsey, Superheating fields of superconductors: Asymptotic analysis and numerical results, *Phys. Rev. B* **53**, 5650 (1996).
- [11] M. K. Transtrum, G. Catelani, and J. P. Sethna, Superheating field of superconductors within ginzburg-landau theory, *Phys. Rev. B* **83**, 094505 (2011).
- [12] D. B. Liarte, M. K. Transtrum, and J. P. Sethna, Ginzburg-landau theory of the superheating field anisotropy of layered superconductors, *Phys. Rev. B* **94**, 144504 (2016).
- [13] G. Catelani and J. P. Sethna, Temperature dependence of the superheating field for superconductors in the high- $\kappa$  london limit, *Phys. Rev. B* **78**, 10.1103/PhysRevB.78.224509 (2008), cited by: 53; All Open Access, Green Open Access.
- [14] F. P.-J. Lin and A. Gurevich, Effect of impurities on the superheating field of type-II superconductors, *Phys. Rev. B* **85**, 10.1103/PhysRevB.85.054513 (2012), cited by: 40; All Open Access, Green Open Access.
- [15] T. Kubo, Superheating fields of semi-infinite superconductors and layered superconductors in the diffusive limit: structural optimization based on the microscopic theory, *Superconductor Science and Technology* **34**, 045006 (2021).
- [16] S. Posen, J. Lee, D. Seidman, A. Romanenko, B. Tennis, O. Melnychuk, and D. Sergatskov, Advances in nb<sub>3</sub>sn superconducting radiofrequency cavities towards first practical accelerator applications, *Superconductor Science and Technology* **34**, 10.1088/1361-6668/abc7f7 (2021), cited by: 19; All Open Access, Green Open Access, Hybrid Gold Open Access.
- [17] G. Müller, H. Piel, J. Pouryamout, P. Boccard, and P. Kneisel, Proceedings of the workshop on thin film coating methods for superconducting accelerating cavities (2000).
- [18] A. R. Pack, J. Carlson, S. Wadsworth, and M. K. Transtrum, Vortex nucleation in superconductors within time-dependent ginzburg-landau theory in two and three dimensions: Role of surface defects and material inhomogeneities, *Phys. Rev. B* **101**, 144504 (2020).
- [19] J. Carlson, A. Pack, M. K. Transtrum, J. Lee, D. N. Seidman, D. B. Liarte, N. S. Sitaraman, A. Senanian, M. M. Kelley, J. P. Sethna, T. Arias, and S. Posen, Analysis of magnetic vortex dissipation in sn-segregated boundaries in nb<sub>3</sub>Sn superconducting rf cavities, *Phys. Rev. B* **103**, 024516 (2021).
- [20] B. Oripov and S. M. Anlage, Time-dependent ginzburg-landau treatment of rf magnetic vortices in superconductors: Vortex semiloops in a spatially nonuniform magnetic field, *Physical Review E* **101**, 10.1103/PhysRevE.101.033306 (2020), cited by: 13; All Open Access, Bronze Open Access, Green Open Access.
- [21] B. Oripov, T. Bieler, G. Ciovati, S. Calatroni, P. Dhakal, T. Junginger, O. B. Malyshev, G. Terenziani, A.-M. Valente-Feliciano, R. Valizadeh, S. Wilde, and S. M. Anlage, High-frequency nonlinear response of supercon-

- ducting cavity-grade Nb surfaces, *Phys. Rev. Appl.* **11**, 064030 (2019).
- [22] J. Allmaras, A. Kozorezov, B. Korzh, K. Berggren, and M. Shaw, Intrinsic timing jitter and latency in superconducting nanowire single-photon detectors, *Phys. Rev. Appl.* **11**, 034062 (2019).
- [23] M. Jönsson, R. Vedin, S. Gyger, J. A. Sutton, S. Steinhauer, V. Zwiller, M. Wallin, and J. Lidmar, Current crowding in nanoscale superconductors within the ginzburg-landau model, *Phys. Rev. Appl.* **17**, 064046 (2022).
- [24] L. Bishop-Van Horn, E. Mueller, and K. A. Moler, Vortex dynamics induced by scanning squid susceptometry, *Phys. Rev. B* **107**, 224509 (2023).
- [25] L. Bishop-Van Horn, pytdgl: Time-dependent ginzburg-landau in python, *Computer Physics Communications* **291**, 108799 (2023).
- [26] T. J. Rieger, D. J. Scalapino, and J. E. Mercereau, Charge conservation and chemical potentials in time-dependent ginzburg-landau theory, *Phys. Rev. Lett.* **27**, 1787 (1971).
- [27] T. J. Rieger, D. J. Scalapino, and J. E. Mercereau, Time-dependent superconductivity and quantum dissipation, *Phys. Rev. B* **6**, 1734 (1972).
- [28] S. Frota-Pessôa, J. A. Blackburn, and B. B. Schwartz, Short weak link with distinct chemical potentials at the boundary, *Phys. Rev. B* **20**, 993 (1979).
- [29] G. R. Berdiyrov, X. H. Chao, F. M. Peeters, H. B. Wang, V. V. Moshchalkov, and B. Y. Zhu, Magnetoresistance oscillations in superconducting strips: A ginzburg-landau study, *Phys. Rev. B* **86**, 224504 (2012).
- [30] G. Kimmel, A. Glatz, and I. S. Aranson, Phase slips in superconducting weak links, *Phys. Rev. B* **95**, 014518 (2017).
- [31] L. Peng, Y. Hu, Z. Li, K. Deng, Y. Zhu, L. Xu, and Y. Zhou, Finite element treatment of vortex states in 3d mesoscopic cylindrical superconductors in a tilted magnetic field, *Acta Physica Polonica A* **133**, 152 – 156 (2018), cited by: 2; All Open Access, Bronze Open Access.
- [32] K. Arutyunov, D. Golubev, and A. Zaikin, Superconductivity in one dimension, *Physics Reports* **464**, 1 (2008).
- [33] S. Michotte, S. Mátéfi-Tempfli, L. Piraux, D. Y. Vodolazov, and F. M. Peeters, Condition for the occurrence of phase slip centers in superconducting nanowires under applied current or voltage, *Phys. Rev. B* **69**, 094512 (2004).
- [34] S. Posen, N. Valles, and M. Liepe, Radio frequency magnetic field limits of nb and nb<sub>3</sub>Sn, *Phys. Rev. Lett.* **115**, 047001 (2015).
- [35] Y. Trenikhina, S. Posen, A. Romanenko, M. Sardela, J.-M. Zuo, D. L. Hall, and M. Liepe, Performance-defining properties of nb<sub>3</sub>Sn coating in srf cavities, *Superconductor Science and Technology* **31**, 015004 (2017).
- [36] J. Lee, S. Posen, Z. Mao, Y. Trenikhina, K. He, D. L. Hall, M. Liepe, and D. N. Seidman, Atomic-scale analyses of nb<sub>3</sub>Sn on nb prepared by vapor diffusion for superconducting radiofrequency cavity applications: a correlative study, *Superconductor Science and Technology* **32**, 024001 (2018).
- [37] U. Pudasaini, G. V. Ereameev, J. W. Angle, J. Tuggle, C. E. Reece, and M. J. Kelley, Growth of Nb<sub>3</sub>Sn coating in tin vapor-diffusion process, *Journal of Vacuum Science & Technology A* **37**, 051509 (2019), [https://pubs.aip.org/avs/jva/article-pdf/doi/10.1116/1.5113597/13962261/051509\\_1\\_online.pdf](https://pubs.aip.org/avs/jva/article-pdf/doi/10.1116/1.5113597/13962261/051509_1_online.pdf).
- [38] J. Lee, Z. Mao, K. He, Z. H. Sung, T. Spina, S.-I. Baik, D. L. Hall, M. Liepe, D. N. Seidman, and S. Posen, Grain-boundary structure and segregation in nb<sub>3</sub>Sn coatings on nb for high-performance superconducting radiofrequency cavity applications, *Acta Materialia* **188**, 155 (2020).
- [39] S.-H. Oh, D. Seol, Y.-J. Jeong, S.-H. Na, J. Kim, W.-S. Ko, J. B. Jeon, and B.-J. Lee, Diffusion in a15 nb<sub>3</sub>Sn: An atomistic study, *Acta Materialia* **234**, 118050 (2022).
- [40] C. Becker, S. Posen, N. Groll, R. Cook, C. M. Schlepütz, D. L. Hall, M. Liepe, M. Pellin, J. Zasadzinski, and T. Proslir, Analysis of Nb<sub>3</sub>Sn surface layers for superconducting radio frequency cavity applications, *Applied Physics Letters* **106**, 082602 (2015), [https://pubs.aip.org/aip/apl/article-pdf/doi/10.1063/1.4913617/13593886/082602\\_1\\_online.pdf](https://pubs.aip.org/aip/apl/article-pdf/doi/10.1063/1.4913617/13593886/082602_1_online.pdf).
- [41] E. Viklund, J. Lee, D. Seidman, and S. Posen, Three-dimensional reconstruction of nb<sub>3</sub>Sn films by focused ion beam cross sectional microscopy, *IEEE Transactions on Applied Superconductivity* **33**, 10.1109/TASC.2023.3257819 (2023), cited by: 0.
- [42] J. K. Freericks, A. Y. Liu, A. Quandt, and J. Geerk, Nonconstant electronic density of states tunneling inversion for a15 superconductors: nb<sub>3</sub>Sn, *Phys. Rev. B* **65**, 224510 (2002).
- [43] W. Markiewicz, Elastic stiffness model for the critical temperature *t<sub>c</sub>* of nb<sub>3</sub>Sn including strain dependence, *Cryogenics* **44**, 767 (2004).
- [44] M. G. T. Mentink, M. M. J. Dhalle, D. R. Dietderich, A. Godeke, F. Hellman, and H. H. J. ten Kate, The effects of disorder on the normal state and superconducting properties of nb<sub>3</sub>Sn, *Superconductor Science and Technology* **30**, 025006 (2016).
- [45] M. M. Kelley, N. S. Sitaraman, and T. A. Arias, Ab initio theory of the impact of grain boundaries and substitutional defects on superconducting nb<sub>3</sub>Sn, *Superconductor Science and Technology* **34**, 015015 (2020).
- [46] N. S. Sitaraman, M. M. Kelley, R. D. Porter, M. U. Liepe, T. A. Arias, J. Carlson, A. R. Pack, M. K. Transtrum, and R. Sundaraman, Effect of the density of states at the fermi level on defect free energies and superconductivity: A case study of nb<sub>3</sub>Sn, *Phys. Rev. B* **103**, 115106 (2021).
- [47] A. E. Koshelev, I. A. Sadovskyy, C. L. Phillips, and A. Glatz, Optimization of vortex pinning by nanoparticles using simulations of the time-dependent ginzburg-landau model, *Phys. Rev. B* **93**, 060508 (2016).
- [48] I. Sadovskyy, A. Koshelev, C. Phillips, D. Karpayev, and A. Glatz, Stable large-scale solver for ginzburg-landau equations for superconductors, *Journal of Computational Physics* **294**, 639 (2015).
- [49] M. P. Sørensen, N. F. Pedersen, and M. Ögren, The dynamics of magnetic vortices in type ii superconductors with pinning sites studied by the time dependent ginzburg-landau model, *Physica C: Superconductivity and its Applications* **533**, 40 (2017).
- [50] S. J. Chapman, C. M. Elliott, A. K. Head, S. D. Howison, F. M. Leslie, J. R. Ockendon, J. Deang, Q. Du, M. Gunzburger, and J. Peterson, Vortices in superconductors: modelling and computer simulations, *Philosophical Transactions of the Royal Society of London. Series A: Mathematical, Physical and Engineering Sciences*

- 355**, 1957 (1997).
- [51] A. Al Luhaibi, A. Glatz, and J. B. Ketterson, Driven responses of periodically patterned superconducting films, *Phys. Rev. B* **106**, 224516 (2022).
- [52] V. L. Ginzburg and L. D. Landau, On the theory of superconductivity, in *On Superconductivity and Superfluidity: A Scientific Autobiography* (Springer Berlin Heidelberg, Berlin, Heidelberg, 2009) pp. 113–137.
- [53] A. Schmid, A time dependent ginzburg-landau equation and its application to the problem of resistivity in the mixed state, *Physik der kondensierten Materie* **5**, 302 (1966).
- [54] L. Gor'Kov and G. Eliashberg, Generalization of the ginzburg-landau equations for non-stationary problems in the case of alloys with paramagnetic impurities, *Sov. Phys. JETP* **27**, 328 (1968).
- [55] Q. Du, M. D. Gunzburger, and J. S. Peterson, Analysis and approximation of the ginzburg-landau model of superconductivity, *SIAM Review* **34**, 54–81 (1992).
- [56] N. Kopnin, *Theory of nonequilibrium superconductivity*, Vol. 110 (Oxford University Press, 2001).
- [57] H. Gao and W. Sun, A new mixed formulation and efficient numerical solution of ginzburg-landau equations under the temporal gauge, *SIAM Journal on Scientific Computing* **38**, A1339 (2016), <https://doi.org/10.1137/15M1022744>.
- [58] Q. Du, Global existence and uniqueness of solutions of the time-dependent ginzburg-landau model for superconductivity, *Applicable Analysis* **53**, 1 (1994).
- [59] M. S. Alnæs, J. Blechta, J. Hake, A. Johansson, B. Kehlet, A. Logg, C. Richardson, J. Ring, M. E. Rognes, and G. N. Wells, The fenics project version 1.5, *Archive of Numerical Software* **3**, 9 (2015).
- [60] M. Tinkham, Viscous flow of flux in type-II superconductors, *Phys. Rev. Lett.* **13**, 804 (1964).
- [61] C. J. Gorter and H. Casimir, On supraconductivity i, *Physica* **1**, 306 (1934).
- [62] H. London, Production of heat in supraconductors by alternating currents, *Nature* **133**, 497 (1934).
- [63] J. Halbritter, On surface resistance of superconductors, *Zeitschrift für Physik* **266**, 209 (1974).
- [64] J. Turneaure, J. Halbritter, and H. Schwettman, The surface impedance of superconductors and normal conductors: The mattis-bardeen theory, *Journal of Superconductivity* **4**, 341 (1991).
- [65] D. C. Mattis and J. Bardeen, Theory of the anomalous skin effect in normal and superconducting metals, *Physical Review* **111**, 412 (1958).
- [66] A. Abrikosov, L. Gor'Kov, and I. Khalatnikov, A superconductor in a high frequency field, *Sov. Phys. JETP* **35**, 182 (1959).
- [67] A. Gurevich, Theory of rf superconductivity for resonant cavities, *Superconductor Science and Technology* **30**, 034004 (2017).
- [68] A. Gurevich and T. Kubo, Surface impedance and optimum surface resistance of a superconductor with an imperfect surface, *Phys. Rev. B* **96**, 184515 (2017).
- [69] B. Aune, R. Bandelmann, D. Bloess, B. Bonin, A. Bosotti, M. Champion, C. Crawford, G. Deppe, B. Dwersteg, D. A. Edwards, H. T. Edwards, M. Ferrario, M. Fouaidy, P.-D. Gall, A. Gamp, A. Gössel, J. Graber, D. Hubert, M. Hüning, M. Juillard, T. Junquera, H. Kaiser, G. Kreps, M. Kuchnir, R. Lange, M. Leenen, M. Liepe, L. Lilje, A. Matheisen, W.-D. Möller, A. Mosnier, H. Padamsee, C. Pagani, M. Pekeler, H.-B. Peters, O. Peters, D. Proch, K. Rehlich, D. Reschke, H. Safa, T. Schilcher, P. Schmüser, J. Sekutowicz, S. Simrock, W. Singer, M. Tigner, D. Trines, K. Twarowski, G. Weichert, J. Weisend, J. Wojtkiewicz, S. Wolff, and K. Zapfe, Superconducting tesla cavities, *Phys. Rev. ST Accel. Beams* **3**, 092001 (2000).
- [70] N. W. Ashcroft and N. D. Mermin, *Solid State Physics* (Holt, Rinehart and Winston, New York, 1976).
- [71] C. Geuzaine and J.-F. Remacle, Gmsh: A 3-d finite element mesh generator with built-in pre- and post-processing facilities, *International journal for numerical methods in engineering* **79**, 1309 (2009).
- [72] E. Viklund, D. N. Seidman, D. Burk, and S. Posen, Improving nb3sn cavity performance using centrifugal barrel polishing (2023), arXiv:2305.10226 [physics.acc-ph].
- [73] M. Tinkham, *Introduction to Superconductivity* (Courier Corporation, 2004).
- [74] L. Kramer and R. J. Watts-Tobin, Theory of dissipative current-carrying states in superconducting filaments, *Phys. Rev. Lett.* **40**, 1041 (1978).
- [75] T. Proslir, J. F. Zasadzinski, L. Cooley, C. Antoine, J. Moore, J. Norem, M. Pellin, and K. E. Gray, Tunneling study of cavity grade nb: Possible magnetic scattering at the surface, *Applied Physics Letters* **92**, 212505 (2008), <https://doi.org/10.1063/1.2913764>.
- [76] T. Kubo and A. Gurevich, Field-dependent nonlinear surface resistance and its optimization by surface nanostructuring in superconductors, *Phys. Rev. B* **100**, 064522 (2019).